ITGB6 modulates resistance to anti-CD276 therapy in head and neck cancer by promoting PF4+ macrophage infiltration

Caihua Zhang[1]*, Kang Li[1]*, Hongzhang Zhu[1]*, Maosheng Cheng[1]*, Shuang Chen[1], Rongsong Ling[2], Cheng Wang[3], Demeng Chen[1#]

1. Otorhinolaryngology Hospital, The First Affiliated Hospital, Sun Yat-sen University, 58 Zhongshan Road II, Guangzhou, Guangdong, 510080, China.
2. Institute for Advanced Study, Shenzhen University, Shenzhen, 518057, China.
3. Hospital of Stomatology, Guangdong Provincial Key Laboratory of Stomatology, Guanghua School of Stomatology, Sun Yat-Sen University, Guangzhou, 510055, China.

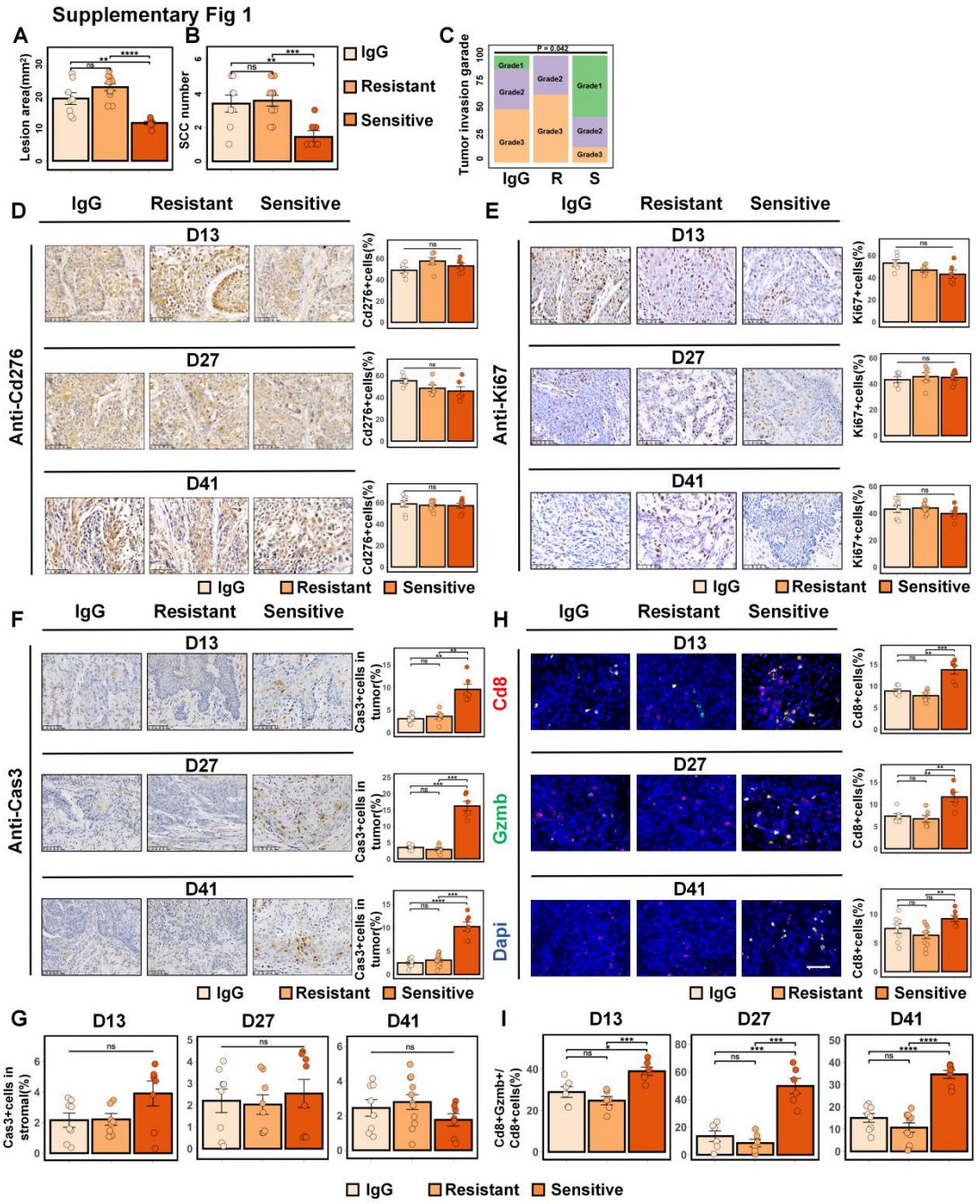

Supplementary Fig1. Detection of relevant indicators in CD276 antibody treatment resistant and sensitive mice, Related to Figure 1

A and B. Quantification of tongue lesion area (A) and SCC number (B) in in different treatment groups. Data are presented as mean ± SD (IgG=8, Resistant=11, Sensitive=7 mice). *P* values were calculated by one-way ANOVA with Tukey's multiple comparison test.

C. Quantification of primary tumor incidence in in different treatment groups (IgG=8, Resistant=11, Sensitive=7 mice). *P* value was calculated by Pearson chi-square test.

D-G. Representative images of CD276 (D), KI67 (E), and Caspase-3 (F) IHC staining (left) and quantification of percentage of $CD276^+$ (D), $KI67^+$ (E), and $Caspase\text{-}3^+$ (F and G) cells (right) in different treatment groups and time points. Scale bar, 100μm. Data are presented as mean ± SD (Day 41 IgG=8, Resistant=11, Sensitive=7, Day 13 and 27 n=6 mice). *P* values are presented by one-way ANOVA with Tukey's multiple comparison test.

H and I. Representative immunofluorescence (IF) staining images of CD8 (green) and GZMB (red) (H). Statistical analysis of the ratio of $CD8^+$ cells and $CD8^+$ $GZMB^+$ cells to $CD8^+$ cells (CD8T killing capacity) (I) in different treatment groups. Scale bar, 25μm. Data are expressed as mean ± SD (Day 41 IgG=8, Resistant=11, Sensitive=7, Day 13 and 27 n=6 mice). *P* values are presented by one-way ANOVA with Tukey's multiple comparison test. Source data and exact p values are provided as a Source Data file.

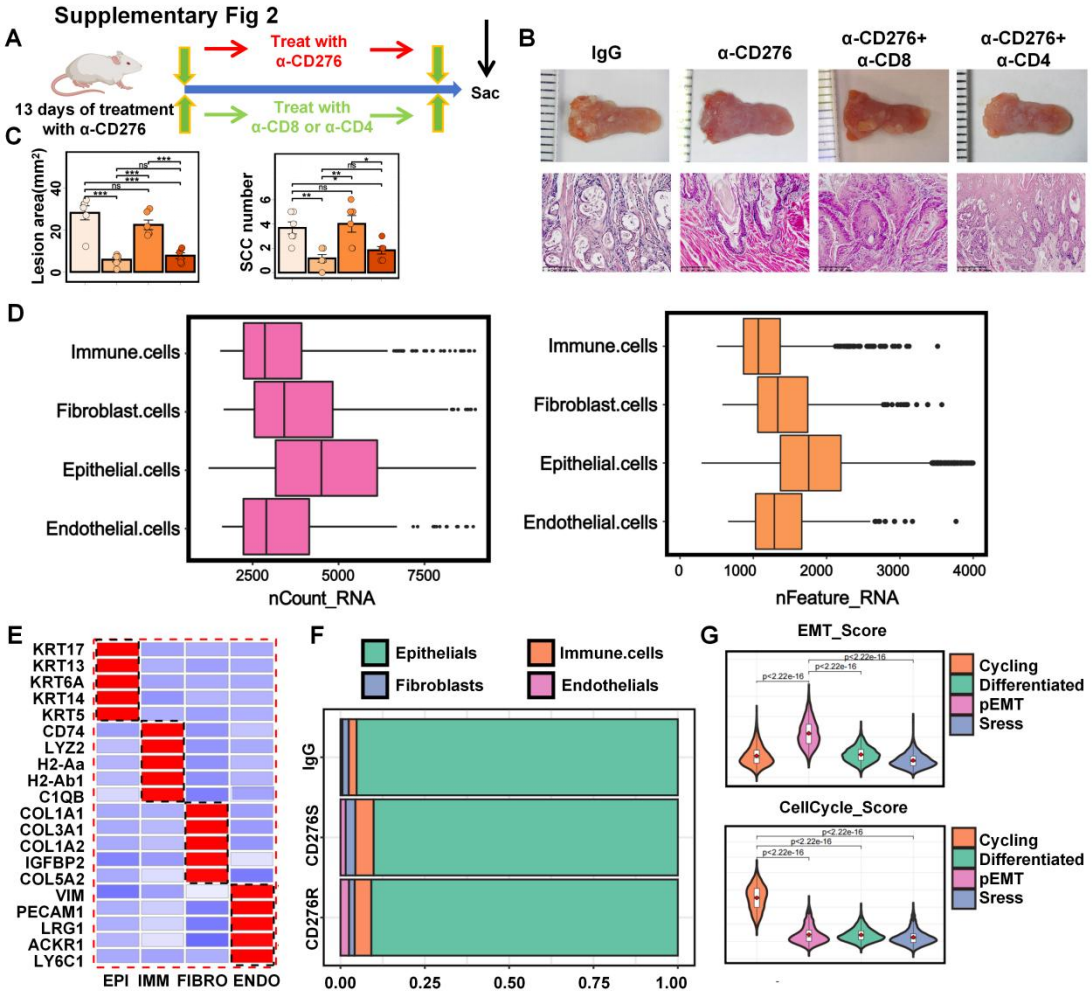

Supplementary Fig2. Assessment of CD4 and CD8 antibody blockade and single-cell sequencing analysis in different mouse groups, Related to Figure 1

A. The experimental design of the HNSCC tumorigenesis model and treatment strategy.

B. Representative images of 4NQO induced HNSCC (upper) and corresponding HE staining (lower) in different treatment groups (n=6 mice). Scale bar, 1mm (upper), 100μm (lower).

C. Quantification of tongue lesion area (left) and SCC number (right) in different treatment groups. Data are presented as mean ± SD (n=6 mice). *P* values are presented by one-way ANOVA with Tukey's multiple comparison test.

D. Box plots of the number of UMIs (left) and genes(right) in the four cell clusters (IgG=6, Resistant=3, Sensitive=3 mice).

E. Heatmap of characteristic genes in epithelial cells (Epi), immune cells (Imm),

fibroblast cells (Fibro), and endothelial cells (Endo). Each cell cluster is represented by five specifically expressed genes (IgG=6, Resistant=3, Sensitive=3 mice).

F. Bar graph showing proportion of single cell clusters in the different treatment groups (IgG=6, Resistant=3, Sensitive=3 mice).

G. Vlnplots of EMT scores and CellCycle scores across subclusters (IgG=6, Resistant=3, Sensitive=3 mice). Source data and exact p values are provided as a Source Data file.

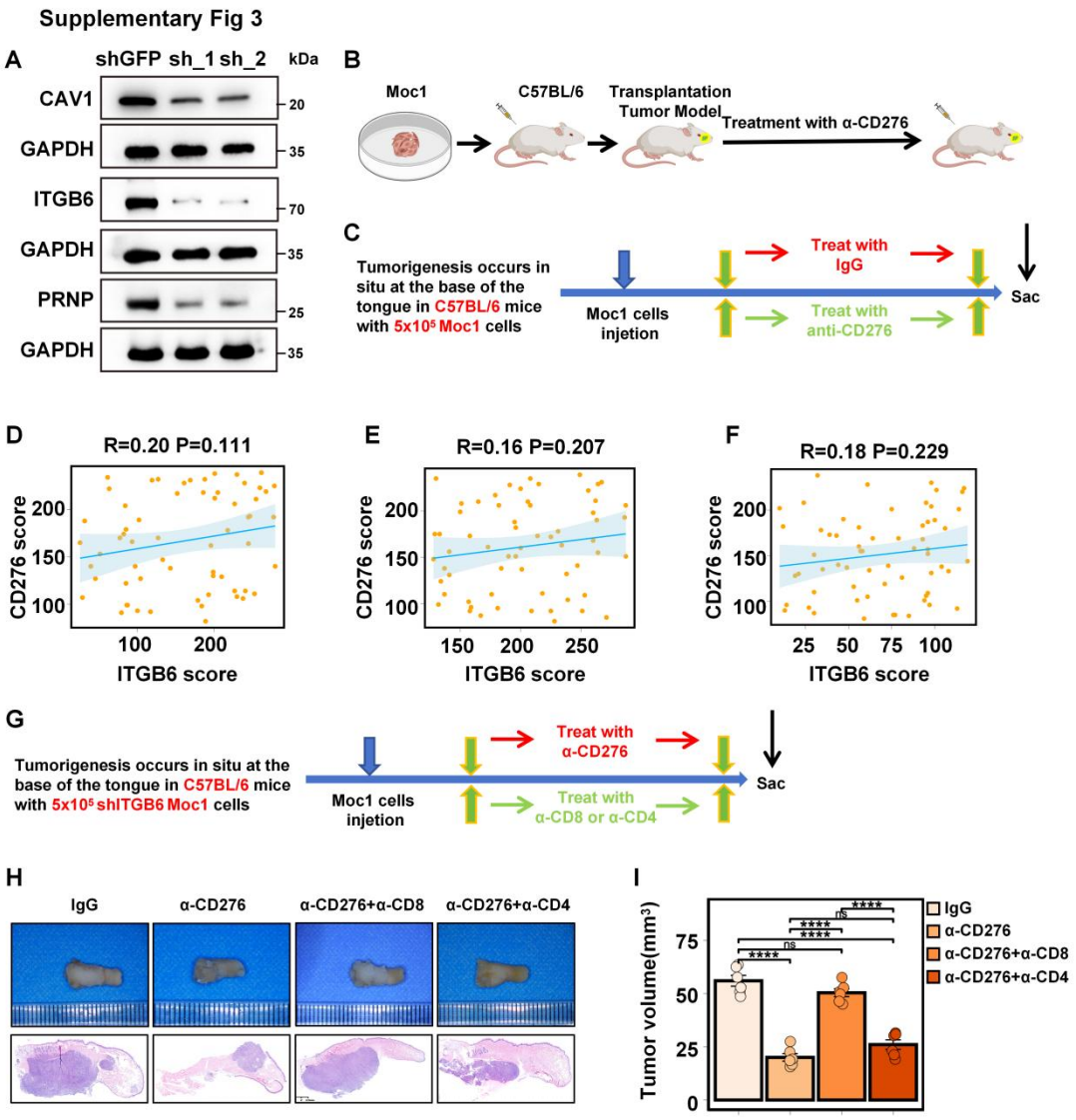

Supplementary Fig3. ITGB6 is a crucial gene that mediates divergent responses to α-CD276 treatment, Related to Figure 2

A. The knockout efficiency of CAV1、ITGB6 and PRNP were validated in Moc1 cell line by WB analysis (n=3 biological replicates).

B and C. Experimental design for the transplantation model and treatment procedure. The C57BL/6 mice, which injected with Moc1 cells, received either the Anti-CD276 antibody or control IgG treatment.

D-F. Correlation of ITGB6 score with CD276 score in IgG, Resistant and Sensitive groups (n=62 mice). *P* values were calculated by Pearson's correlation analysis.

G. Experimental design for the transplantation model and treatment procedure. The C57BL/6 mice, which injected with shITGB6 Moc1 cells, received either α-CD8 or

α-CD4 treatment with α-CD276 treatment.

H. Representative images of HNSCC in situ (upper) and corresponding HE staining (down) in different treatment groups (n=6 mice). Scale bar, 1mm (upper), 100μm (down).

I. Quantification of tumor volume in different treatment groups. Data are presented as mean ± SD (n=6 mice). *P* values are presented by one-way ANOVA with Tukey's multiple comparison test. Source data and exact p values are provided as a Source Data file.

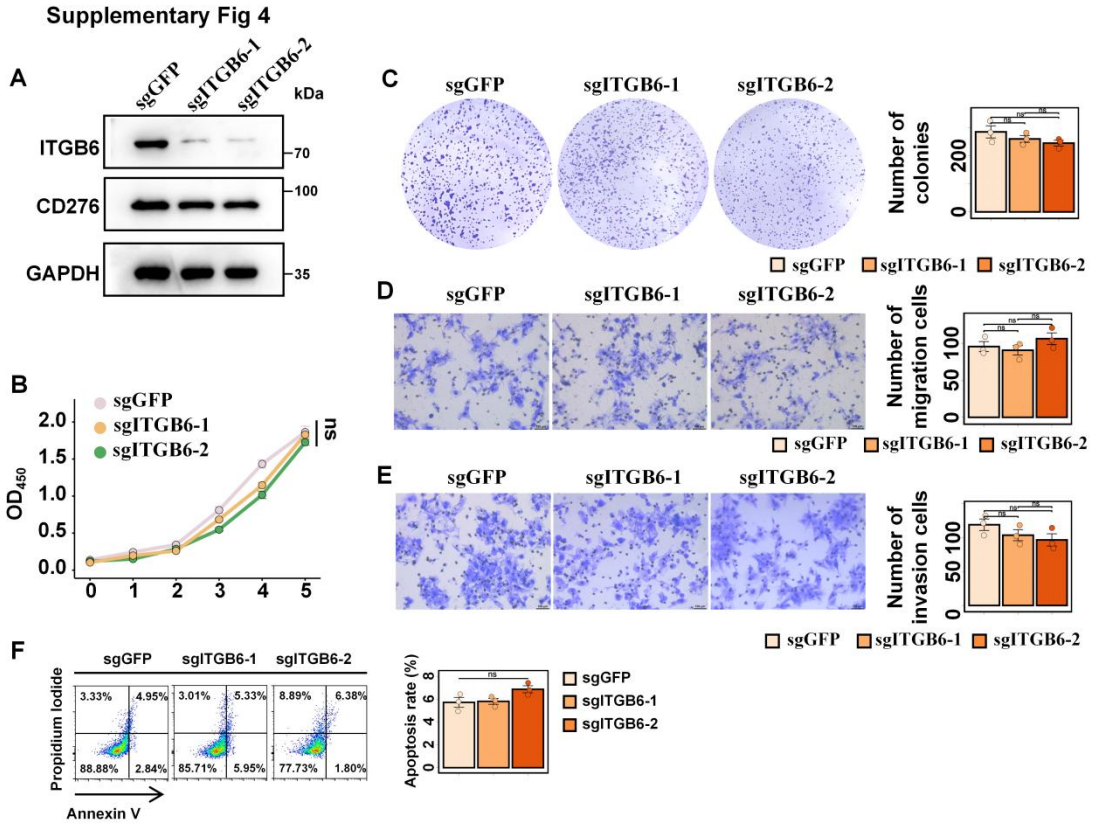

Supplementary Fig4. ITGB6 does not significantly influence tumor cell migration, invasion, or proliferation capabilities, Related to Figure 2

A. Western blot of ITGB6 and CD276 in ITGB6 KO and control HNSCC cells (n=3 biological replicates).

B. CCK8 assay of cell proliferation in ITGB6 KO and control HNSCC cells (n=3 biological replicates).

C. Representative images (left) and quantitative analysis (right) of colony formation

in ITGB6 KO and control HNSCC cells. Data are presented as mean ± SD (n=3 biological replicates).

D. Representative images (left) and quantitative analysis (right) of Transwell migration in ITGB6 KO and control HNSCC cells. Scale bar, 100 mm. Data are presented as mean ± SD (n=3 biological replicates).

E. Representative images (left) and quantitative analysis (right) of Transwell invasion in ITGB6 KO and control HNSCC cells. Scale bar, 100 mm. Data are presented as mean ± SD (n=3 biological replicates).

F. Representative images (left) and quantitative analysis (right) of apoptosis in ITGB6 KO and control HNSCC cells. Data are presented as mean ± SD (n=3 biological replicates). Source data and exact p values are provided as a Source Data file.

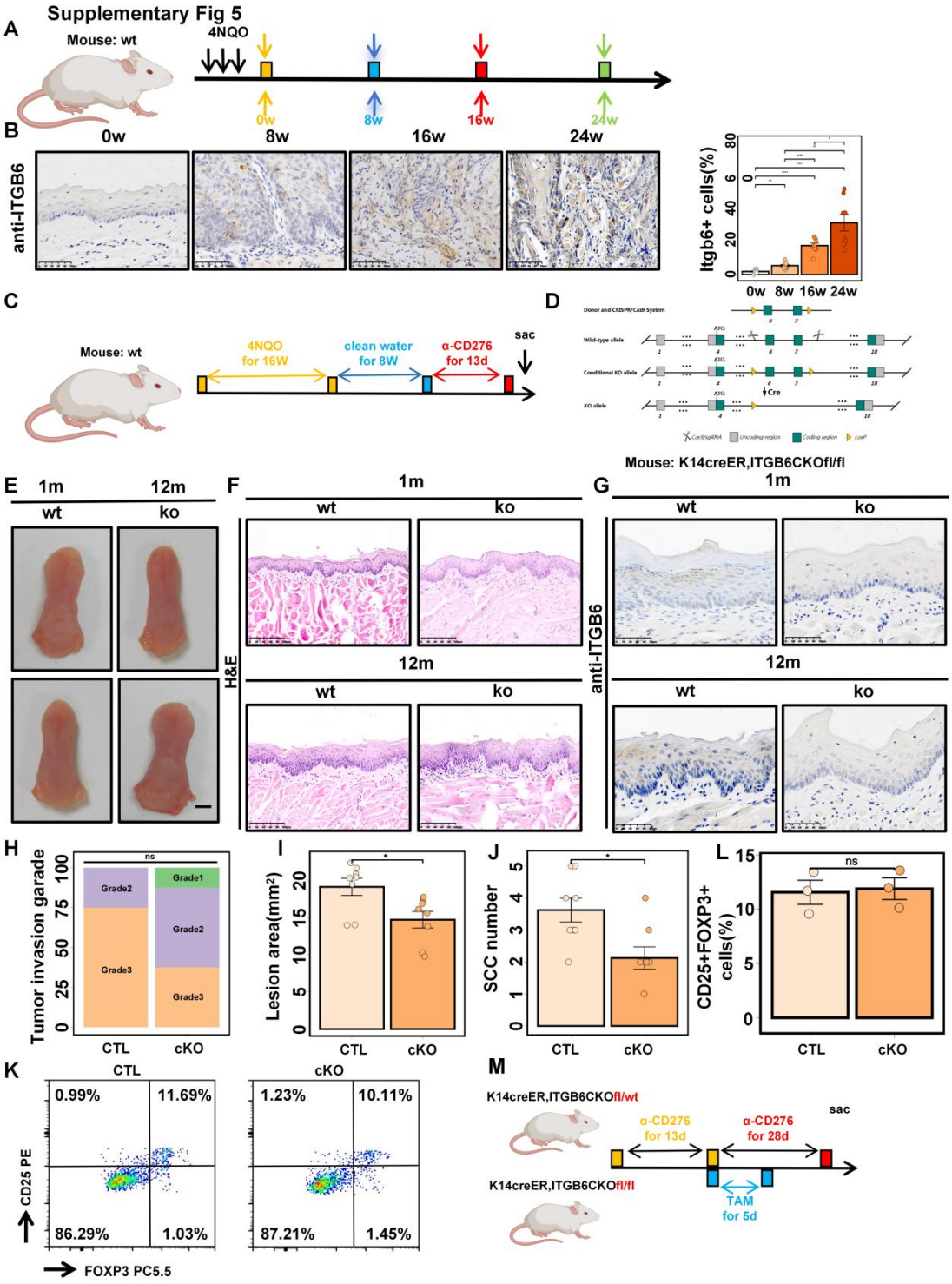

Supplementary Fig5. Knockout of ITGB6 does not affect normal tongue development in mice, Related to Figure 2

A. The experimental design of the HNSCC tumorigenesis model and the schematic diagram of sample collection in batches. w, week.

B. Representative images of ITGB6 IHC staining (left) and percentage of ITGB6^{+} cells (right) at different time points. Scale bar, 100μm. Data are presented as mean ±

SD (n=8 mice). *P* values are presented by two-tailed unpaired Student's t test.

C. The experimental design of the HNSCC tumorigenesis model and the strategy of treatment.

D. Construction of Itgb6-conditional knockout (cKO) mice.

E-G. Representative images of normal tongue (E), H&E staining (F), and ITGB6 IHC staining (G) in CTL and cKO mice at different time points (n=8 mice). m, month. Scale bar, 1mm (E), 100μm (F), 50μm (G).

H. Quantification of primary tumor incidence in CTL and cKO mice (n=8 mice). *P* value was calculated by Pearson chi-square test.

I and J. Quantification of tongue lesion area and SCC number in CTL and cKO mice (n=8 mice). Data are presented as mean ± SD. *P* values were calculated by two-tailed unpaired Student's t-test.

K and L. Representative flow plots show frequency of Tregs (K) and quantification of the proportions of Tregs (L) in CTL and cKO mice (n=3 mice). Data are presented as mean ± SD. *P* values were calculated by two-tailed unpaired Student's t-test.

M. The experimental design of the HNSCC tumorigenesis model and the strategy of treatment. Source data and exact p values are provided as a Source Data file.

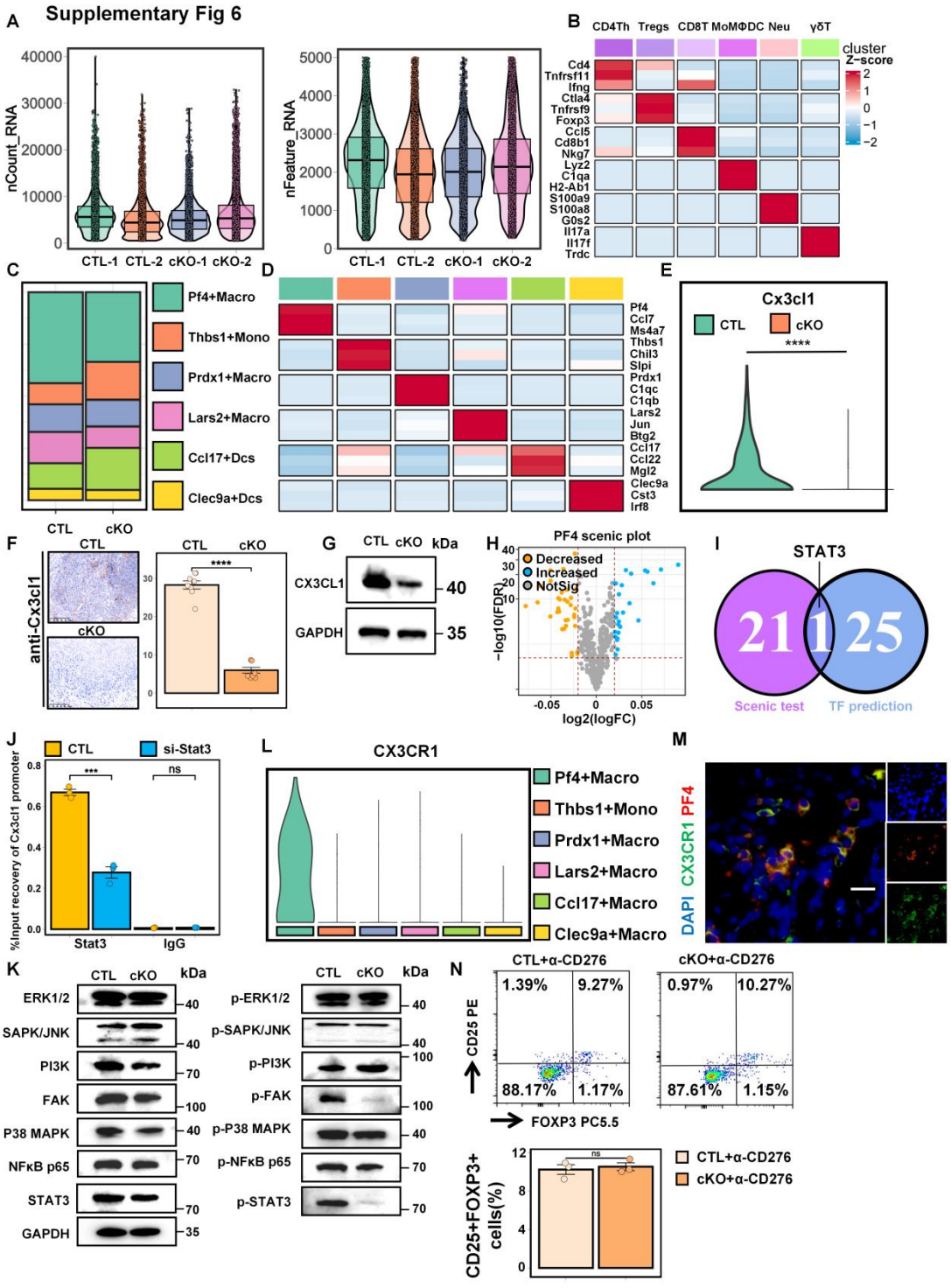

Supplementary Fig6. Single-cell sequencing analysis of ITGB6 knockout combined with CD276 antibody treatment, Related to Figure 4

A. Violin plots of the number of UMIs (left) and genes (right) in the four samples (n=2 mice in each group).

B. Heatmap of signature genes for Immune cells subclusters from mouse HNSCC tumor tissues. Each cell cluster is represented by three specifically expressed genes.

C. The proportions of MoMΦDC subclusters between the two groups.

D. Heatmap of signature genes for MoMΦDC cells subclusters. Each cell cluster is represented by three specifically expressed genes.

E. Violin plot showing the expression of CX3CL1 in epithelial cells between the two groups.

F. Representative images of CX3CL1 IHC staining (left) and quantitation of the percentage of $CX3CL1^{+}$ cells (right) in different treatment groups. Scale bar, 50μm. Data are shown as mean ± SD (n=8 mice). *P* values were calculated by two-tailed unpaired Student's t-test.

G. Western blotting analysis of CX3CL1 in control and cKO mice (n=3 mice).

H. Volcano plot showing differences in transcription factors of tumor cells between the two groups, transcription factors derived from Scenic analysis.

I. Venn diagram showing Stat3 as overlaped transcription factor between Scenic and online analysis.

J. ChIP-qPCR analysis of Stat3 binding to CX3CL1. Data were presented as mean ± SD (n=3 biological replicates). *P* values were calculated by two-tailed unpaired Student's t-test.

K. Western blotting analysis of ERK1/2, SAPK/JNK, PI3K, AKT, FAK, P38 MAPK, NFKB1, STAT3 and analysis of phosphorylated ERK1/2, SAPK/JNK, PI3K, AKT, FAK, P38 MAPK, NFKB1, STAT3 in control and cKO Moc1 cells (n=3 biological replicates).

L. Violin plot showing the expression of Cx3cr1 in all cell types.

M. Immunofluorescence staining to detect expression of mice CX3CR1 (red), and PF4 (green) (n=8 mice). DAPI was used for nuclear staining. Scale bar, 25 μm.

N. Representative flow plots show frequency of Tregs (upper) and quantification of the proportions of Tregs (down) in different treatment groups. Data are presented as mean ± SD (n=3 mice). *P* values were calculated by two-tailed unpaired Student's t-test. Source data and exact p values are provided as a Source Data file.

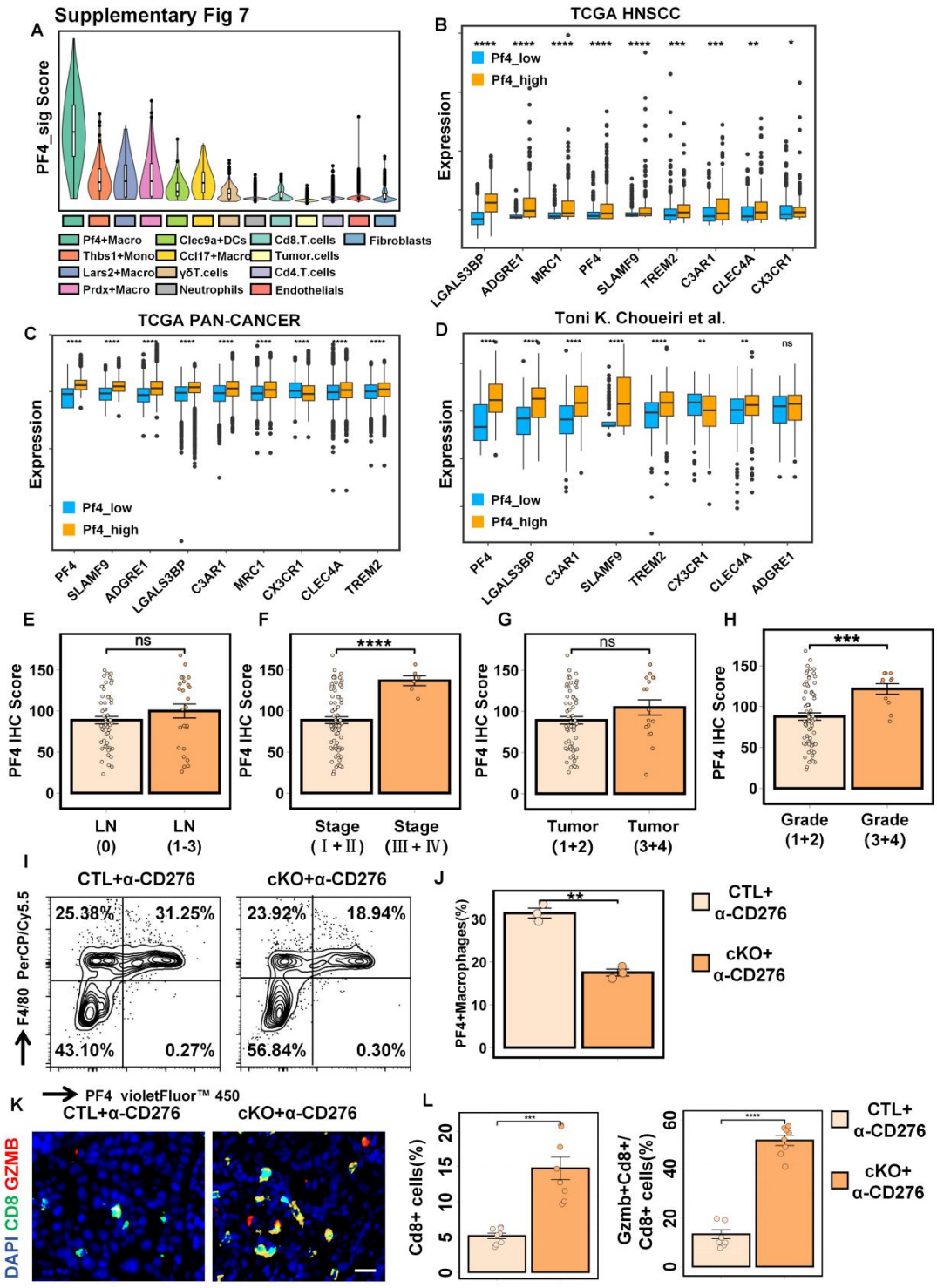

Supplementary Fig7. PF4 macrophages are accompanied by worse survival and less CD8⁺ T-cell infiltration and killing capacity, Related to Figure 5

A. Vlnplot of scores based on PF4 signature across cell populations (n=2 mice in each group).

B. Expression of genes in PF4 signature in pf4_high and PF4_low group with HNSCC (TCGA-Cohort) (n=259 in PF4_low and n=260 in PF4_high).

C. Expression of genes in PF4 signature in pf4_high and PF4_low group with PAN-CANCER (TCGA-Cohort) (n=4892 in PF4_low and n=4892 in PF4_high).

D. Expression of genes in PF4 signature in pf4_high and PF4_low group with renal cancer (GEO-Cohort) (n=155 in PF4_low and n=156 in PF4_high)[1].

E-H. Comparison of PF4 staining score by lymph node metastasis status (E) (n=65 in LN_0 and 16 in LN_{1-3}), tumor stage (F) (n=75 in Stage $_{Ⅰ,Ⅱ}$ and 6 in Stage $_{Ⅲ,Ⅳ}$), T classification (G) (n=64 in $Tumor_{1,2}$ and 17 in $Tumor_{3,4}$), and tumor grade (H) (n=70 in $Grade_{1,2}$ and 11 in $Grade_{3,4}$) of patient from FAH-SYSU-Cohort1. Data are presented as mean ± SD. *P* values were calculated by two-tailed unpaired Student's t-test.

I and J. Representative flow cytometry plots (I) and statistical analysis of $F4/80^+PF4^+$ macrophages (J) in different treatment groups. Data are presented as mean ± SD (n=3 mice). *P* value was calculated by two-tailed unpaired Student's t-test.

K and L. Representative immunofluorescence (IF) staining images of CD8 (green) and GZMB (red) (K). Statistical analysis of the ratio of $CD8^+$ cells (left) and $CD8^+$ $GZMB^+$ cells to $CD8^+$ cells (CD8T killing capacity) (right) in different treatment groups (L). Scale bar, 25μm. Data are expressed as mean ± SD (n=8 mice). *P* value was calculated by two-tailed unpaired Student's t-test. Source data and exact p values are provided as a Source Data file.

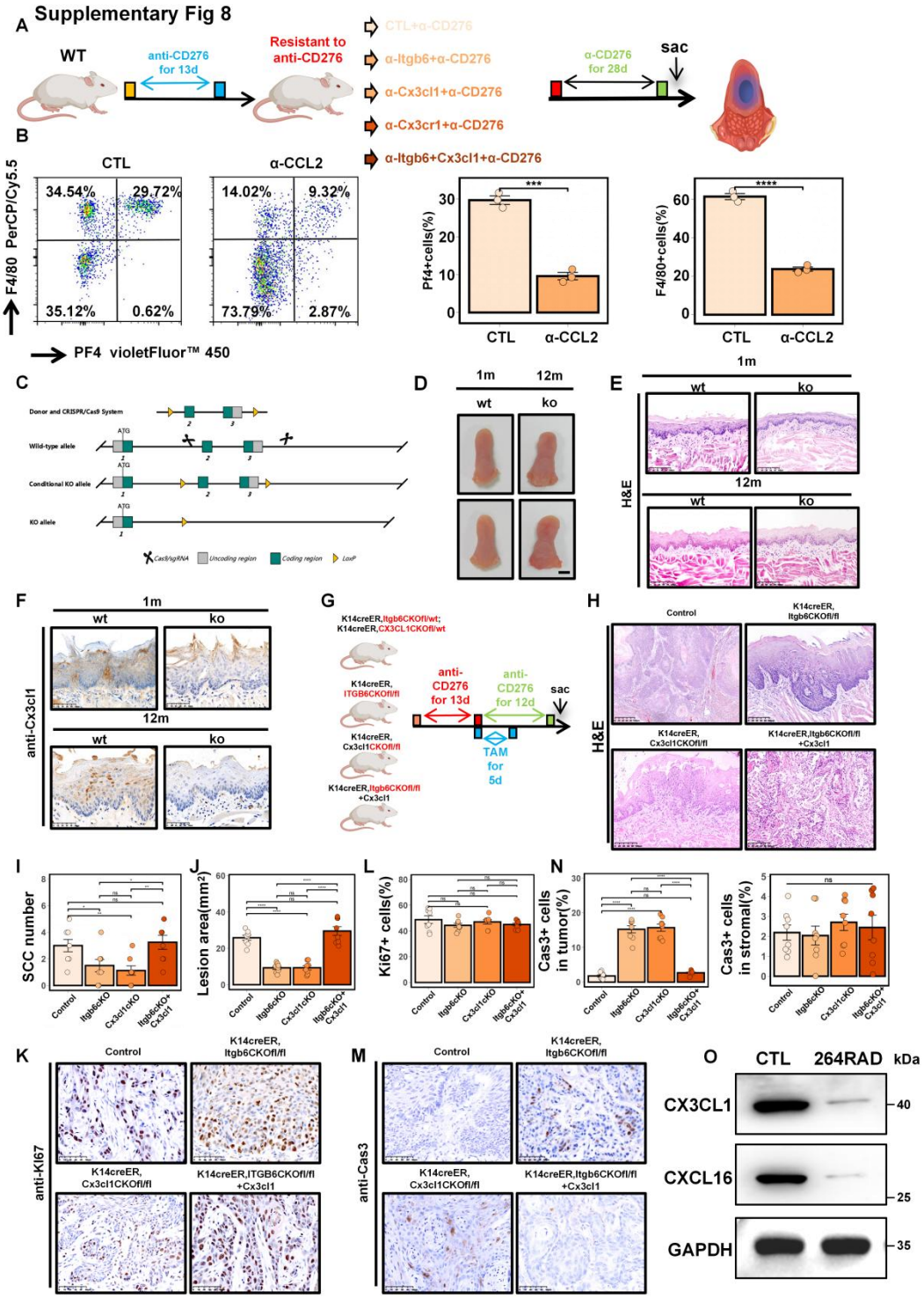

Supplementary Fig8. CX3CL1-CX3CR1 axis is required for PF4$^+$ macrophages recruitment and activation, Related to Figure 6

A. Establishing the mouse model of HNSCC drug resistance and treatment options.

B. Representative flow cytometry plots (left) and statistical analysis of F4/80$^+$PF4$^+$ and F4/80$^+$ macrophages (right) in different treatment groups. Data are presented as mean ± SD (n=3 mice). *P* value was calculated by two-tailed unpaired Student's t-test.

C. Construction of CX3CL1-conditional knockout mice.

D. Representative images of normal tongue in WT (*K14*^{creER}, *CX3CL1*$^{fl/wt}$) and KO (*K14*^{creER}, *CX3CL1*$^{fl/fl}$) mice at different time points. Scale bar, 1mm.

E and F. Representative images of H&E staining (D) and ITGB6 IHC staining (E) in wildtype and KO mice at different time points (n=8 mice). Scale bar, 100μm (D) and 50μm (E).

G. Strategy for the treatment of HNSCC mice.

H. Representative images of H&E in different treatment groups (n=8 mice). Scale bar, 100μm.

I and J. Quantification of tongue lesion area (H) and SCC number (I) in different treatment groups. Data are presented as mean ± SD (n=8 mice). *P* values are presented by one-way ANOVA with Tukey's multiple comparison test.

K-N. Representative images of KI67 (J) and Caspase-3 (L) IHC staining and quantitation of the percentage of KI67^{+} (K) and Caspase3^{+} (M) cells in different treatment groups. Scale bar, 100μm. Data are shown as mean ± SD (n=8 mice). *P* values are presented by one-way ANOVA with Tukey's multiple comparison test.

O. Western blotting analysis of CX3CL1 and CXCL16 in control and 264RAD-treated mice (n=3 mice). Source data and exact p values are provided as a Source Data file.

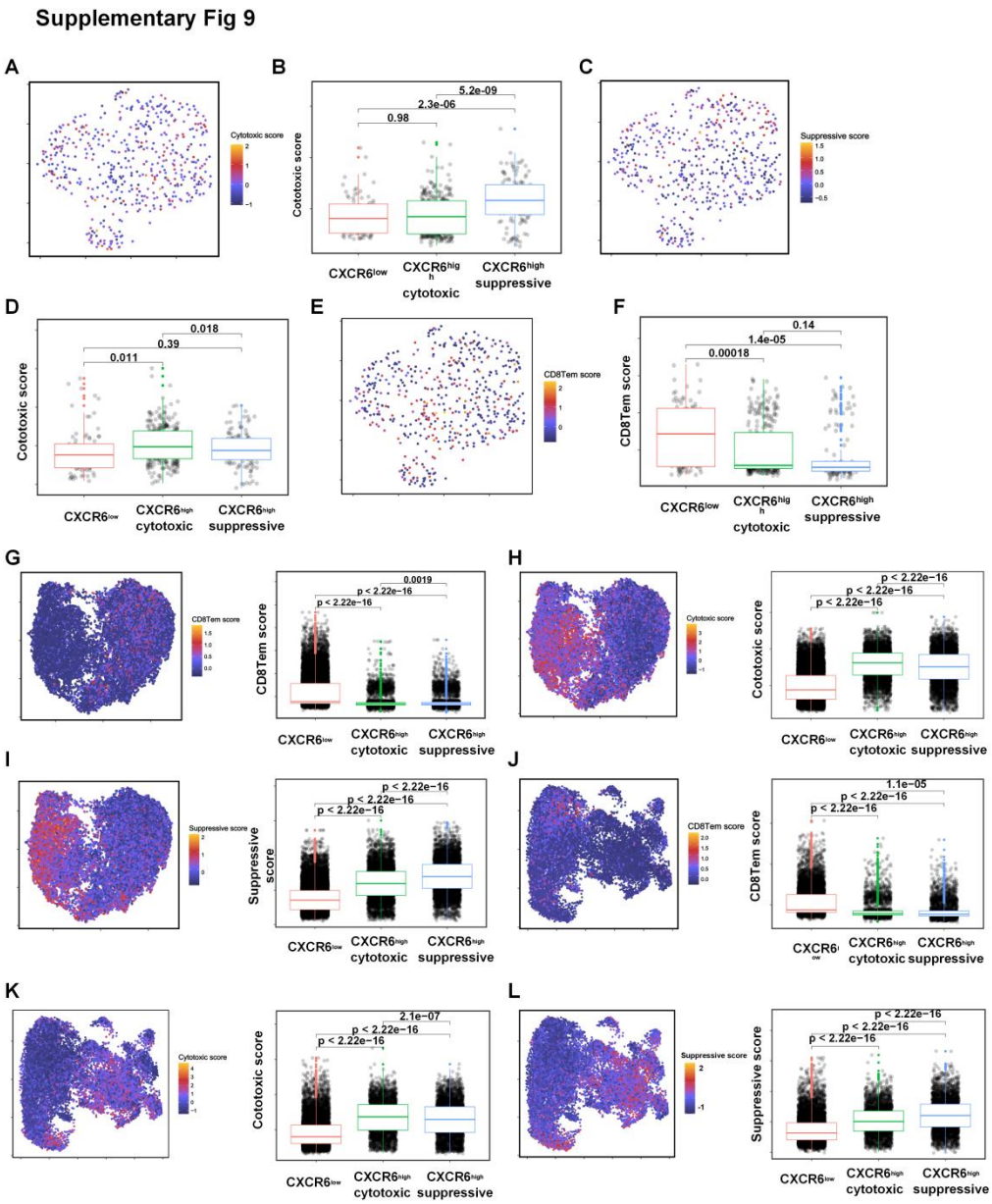

Supplementary Fig9. PF4^{+} macrophages suppress the cytotoxicity and induce the exhaustion of CXCR6^{+} CD8^{+} T cells, Related to Figure 7

A and B. UMAP (A) of cytotoxic score in CD8^{+} T cells with HNSCC and statistical analysis of scores for three CD8^{+} T-cell subclusters (n=2 mice in each group). *P* values are presented by one-way ANOVA with Tukey's multiple comparison test.

C and D. UMAP (A) of suppressive score in CD8^{+} T cells with HNSCC and statistical analysis of scores for three CD8^{+} T-cell subclusters (n=2 mice in each group). *P* values are presented by one-way ANOVA with Tukey's multiple comparison test.

E and F. UMAP (A) of Tem score in CD8^{+} T cells with HNSCC and statistical

analysis of scores for three $CD8^+$ T-cell subclusters (n=2 mice in each group). *P* values are presented by one-way ANOVA with Tukey's multiple comparison test.

G-I. UMAP (left) of cytotoxic (G), suppressive (H) and Tem (I) scores in $CD8^+$ T cells with HNSCC (GEO-Cohort1) and statistical analysis (right) of scores for three $CD8^+$ T-cell subclusters (n=18 biological replicates). Data are presented as mean ± SD. *P* values are presented by one-way ANOVA with Tukey's multiple comparison test.

J-L. UMAP (left) of cytotoxic (J), suppressive (K) and Tem (L) scores in $CD8^+$ T cells with HNSCC (GEO-Cohort2) and statistical analysis (right) of scores for three $CD8^+$ T-cell subclusters (n=63 biological replicates). *P* values are presented by one-way ANOVA with Tukey's multiple comparison test. Source data and exact p values are provided as a Source Data file.

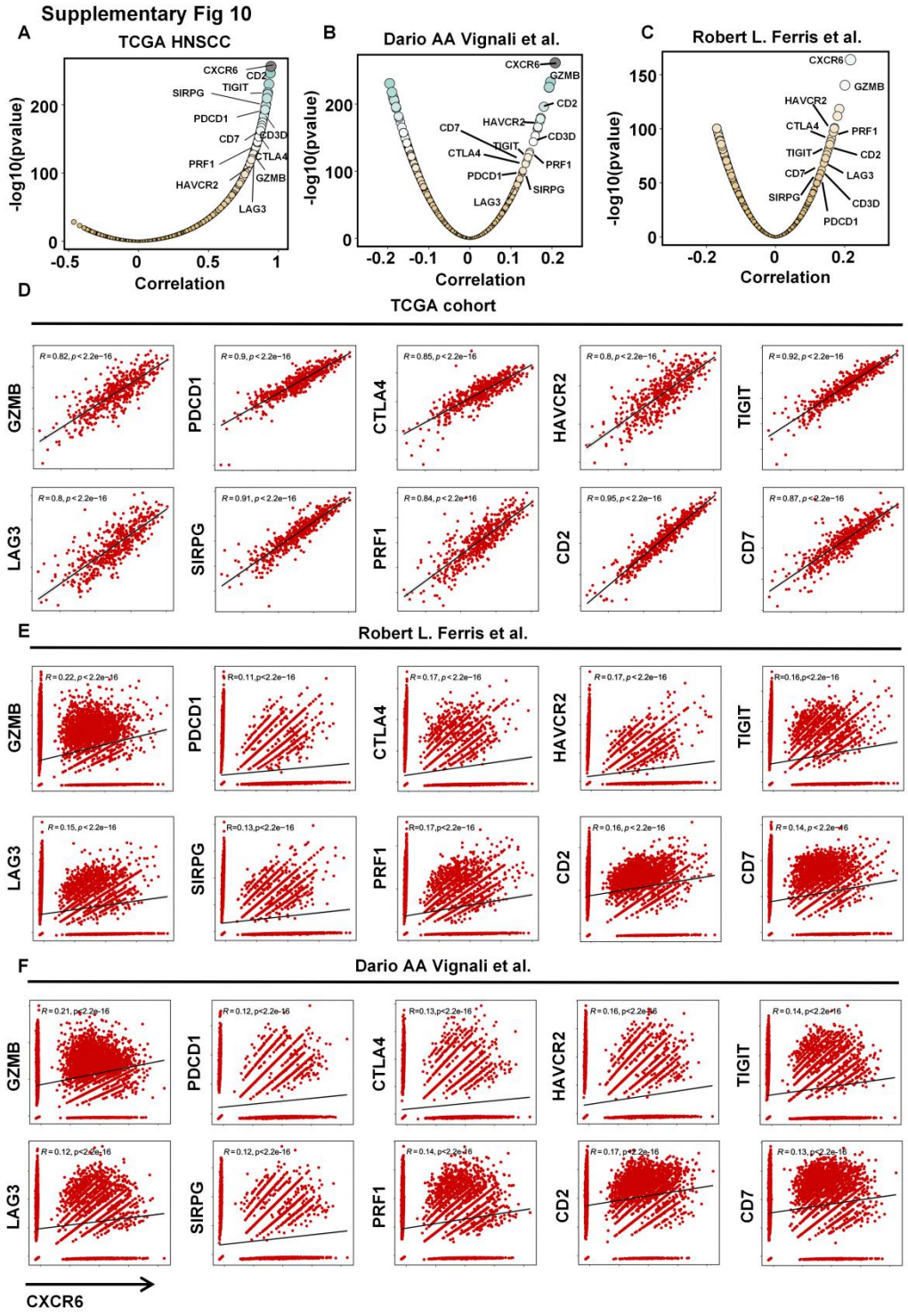

Supplementary Fig10. CXCR6 is positively correlated with both cytotoxic and exhaustion signatures, Related to Figure 8

A-C. Correlation of CXCR6 with the genes in TCGA-Cohort (A) (n=519 biological replicates), GEO-Cohort1 (B) (n=63 biological replicates)[2] and GEO-Cohort2 (C) (n=18 biological replicates)[3]. *P* values were calculated by Pearson's correlation analysis.

D-F. Correlation of genes at the intersection of TCGA-Cohort (D) (R>0.8, p<0.01) (n=519 biological replicates), GEO-Cohort1 (E) (R>0.2, p<0.01) (n=63 biological replicates) and GEO-Cohort2 (F) (R>0.2, p<0.01) (n=18 biological replicates). Source data and exact p values are provided as a Source Data file.

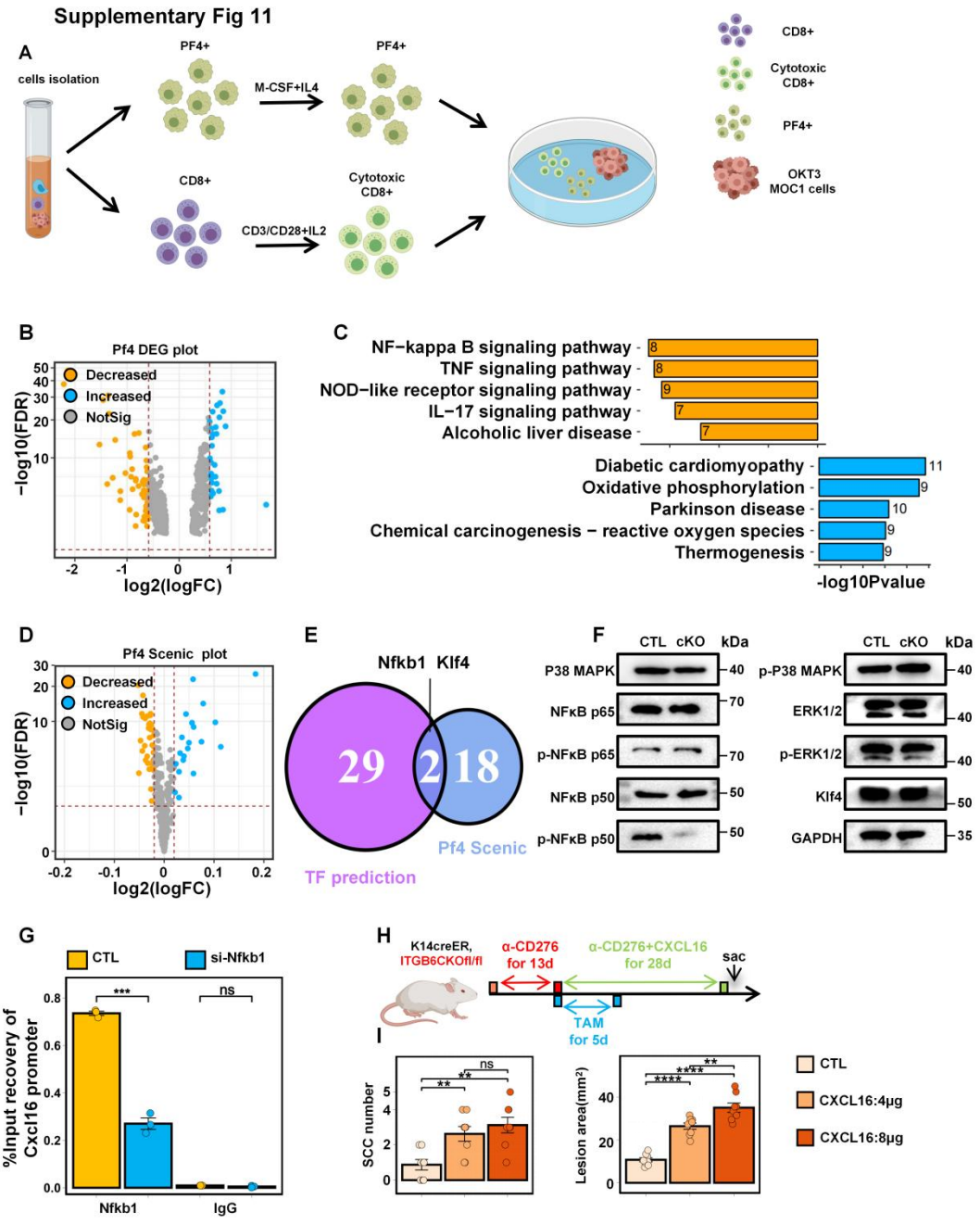

Supplementary Fig11.NFKB1 regulates the expression of CXCL16 in PF4+ macrophages, Related to Figure 8

A. T cell killing experiments include $CD8^+$ T cell sorting and $CD8^+$ T cell activation,

$PF4^+$ Macrophages sorting and $PF4^+$ Macrophages activation, co-culture of $CD8^+$ T cells, $PF4^+$ Macrophages and Moc1 cells.

B. Differential expression analysis identifies differences in $PF4^+$ Macrophages between CTL and cKO mice (n=2 mice in each group). Differential expression analysis by DEseq2. Volcano plots demonstrating significant ($p<0.05$) differential ($|logFC|>0.585$) abundances.

C. KEGG pathway enrichment analysis of differentially expressed genes of $PF4^+$ Macrophages in different groups.

D. Volcano plot showing differences in transcription factors of $PF4^+$ macrophages between the two groups, transcription factors derived from Scenic analysis. The *P* values in Supplementary Data 10 were calculated using the FindAllMarkers function from the Seurat package for single-cell RNA sequencing data analysis. This function identifies differentially expressed genes between clusters by performing the Wilcoxon rank sum test. *P* values are two-sided and exact. Adjustments for multiple comparisons were made using the Bonferroni correction method.

E. Venn diagram showing Nfkb1 and Klf4 as overlapped transcription factors between Scenic and online analysis.

F. Western blotting analysis of P38 MAPK, NFKB P65, NFKB P50, ERK1/2 and KLF4 and analysis of phosphorylated P38 MAPK, NFKB P65, NFKB P50, ERK1/2 and KLF4 in $PF4^+$ macrophages of control and cKO mice (n=3 mice).

G. ChIP-qPCR analysis of Nfkb1 binding to Cxcl16. Data were presented as mean ± SD (n=3 biological replicates). *P* values were calculated by two-tailed unpaired Student's t-test.

H. Diagram of the HNSCC mouse model and treatment strategy.

I. Quantification of tongue SCC number (left) and lesion area (right) in different groups. Data are presented as mean ± SD (n=8 mice). *P* values were calculated by two-tailed unpaired Student's t-test. Source data and exact p values are provided as a Source Data file.

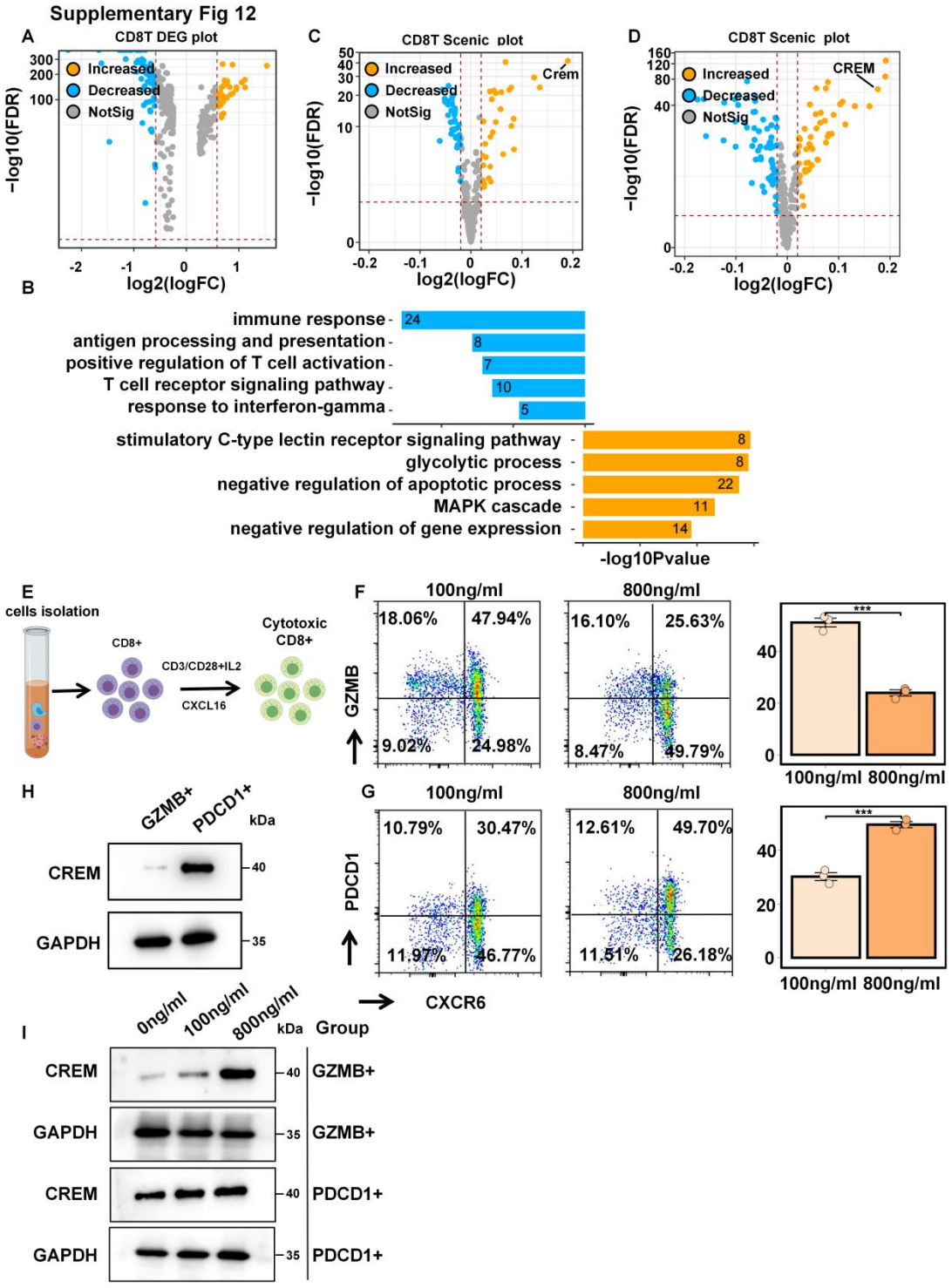

Supplementary Fig12. CREM plays a crucial role in the exhaustion of CXCR6+ CD8+ T cells, Related to Figure 8

A. Differential expression analysis identifies differences in $GZMB^{+}CXCR6^{+}CD8^{+}$T cells and $PDCD1^{+}CXCR6^{+}CD8^{+}$T cells (n=2 mice for CTL and cKO groups). Differential expression analysis by DEseq2. Volcano plots demonstrating significant ($p<0.05$) differential ($|logFC|>0.585$) abundances.

B. GO pathway enrichment analysis of differentially expressed genes of $CD8^+$T cells in different subsets.

C. Volcano plot showing differences in transcription factors of $CD8^+$T cells between the two subsets, transcription factors derived from Scenic analysis.

D. Volcano plot showing differences in transcription factors of $CD8^+$T cells between the two subsets in data from Robert L. Ferris et al, transcription factors derived from Scenic analysis.

E. The experimental design of T cell killing experiments.

F. Representative flow plots show frequency of the $CXCR6^+$ $CD8^+$ $GZMB^+$ T cells (left) and quantification of the proportions of $CXCR6^+$ $CD8^+$ $GZMB^+$ T cells (right) in groups different CXCL16 doses (n=3 biological replicates). *P* values were calculated by two-tailed unpaired Student's t-test.

G. Representative flow plots show frequency of the $CXCR6^+$ $CD8^+$ $PDCD1^+$ T cells (left) and quantification of the proportions of $CXCR6^+$ $CD8^+$ $PDCD1^+$ T cells (right) in groups different CXCL16 doses (n=3 biological replicates). *P* values were calculated by two-tailed unpaired Student's t-test.

H. Western blotting analysis of CREM in different subsets of $CXCR6^+CD8^+$T cells (n=3 biological replicates).

I. Western blot analysis of CREM in different subsets of CXCR6+ CD8+ T cells under various CXCL16 stimulation conditions (n=3 biological replicates). Source data and exact p values are provided as a Source Data file.

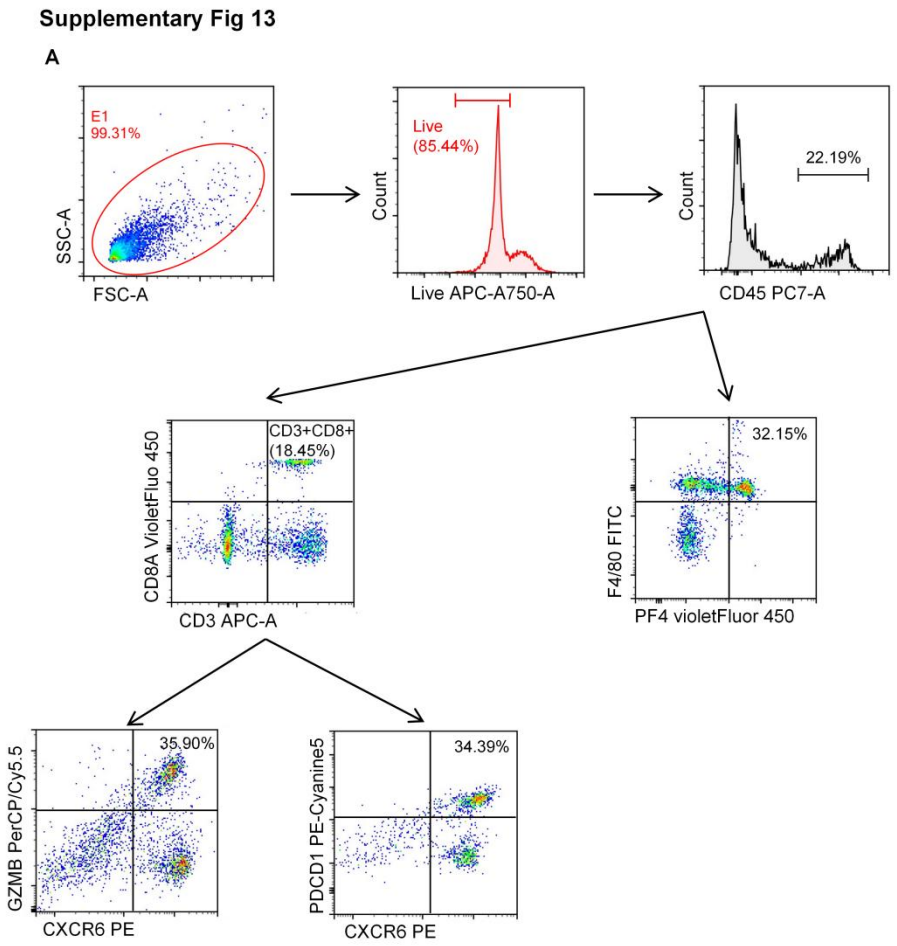

Supplementary Fig13. Flow Cytometry Gating and Sorting Strategies

A. Sequential gating strategy of myeloid cells and lymphocytes from tumor tissue for flow cytometry analysis. Flow cytometry gating strategy for identifying and sorting CXCR6+ CD8+ T cells and PF4+ macrophages. Cells were first gated on forward scatter area (FSC-A) vs. side scatter area (SSC-A) to exclude debris and select live cells. Live cells were then gated using live/dead discrimination (APC-A750-A). CD45+ leukocytes were identified, followed by CD3+CD8+ T cells. The CD3+CD8+ T cells were further subdivided into GZMB+ CXCR6+ and PDCD1+ CXCR6+ populations. Concurrently, PF4+ F4/80+ macrophages were also identified. Source data and exact p values are provided as a Source Data file.

Reference

1. Braun, D.A. et al. Interplay of somatic alterations and immune infiltration modulates response to PD-1 blockade in advanced clear cell renal cell carcinoma. *Nat Med* **26**, 909-918 (2020).

2. Kurten, C.H.L. et al. Investigating immune and non-immune cell interactions in head and neck tumors by single-cell RNA sequencing. *Nat Commun* **12**, 7338 (2021).
3. Cillo, A.R. et al. Immune Landscape of Viral- and Carcinogen-Driven Head and Neck Cancer. *Immunity* **52**, 183-199 e189 (2020).